Proceedings of the 12th International Workshop on Wave Hindcasting and Forecasting and 3rd Coastal Hazards Symposium, Hawaii, 30 Oct – 4 Nov 2011

Implementation of the Spherical Multiple-Cell Grid in the Global Wave Model ─ WAVEWATCH III

Jian-Guo Li*

Met Office, Exeter EX1 3PB, United Kingdom

Abstract: A spherical multiple-cell (SMC) grid has been implemented into the UK Met Office version of WAVEWATCH III global wave model. The SMC grid is an unstructured grid but retains the lat-lon grid cells and hence preserves the simplicity of finite-difference on rectangular cells. The SMC grid relaxes the CFL restriction at high latitudes by zonally merging the lat-lon cells. It also allows all land points to be removed out of the wave model, leading to a 45% reduction of advection computation for each time step. The combined reduction of advection computation cost is about 80% in comparison with that of the standard lat-lon grid propagation scheme. Four terms, advection, diffusion, refraction and great-circle turning (GCT) are formulated on the SMC grid. The advection term is discretised with an upstream non-oscillatory 2nd order (UNO2) scheme, which is about 30% faster than the 3rd order scheme in the original model. The rotation by refraction and GCT is represented by a simple rotation scheme so that the maximum rotation angle is no longer limited within one direction bin width. The overall computing time is reduced by 1/3 in comparison with the standard lat-lon grid global wave model, using the same 2nd order advection scheme. Validations with altimeter SWH observations and NDBC buoy spectra have confirmed that the SMC grid wave model performs as accurately as the standard lat-lon grid model. The SMC grid also allows refined resolution at coastlines and around small islands within the same model. This is a desirable feature for wave models as the blocking effect of small islands is important sink of ocean surface waves. A 3-tiered (6-12-25 km) SMC grid is used to demonstrate the refined resolution effect on global ocean surface wave propagation, including the Arctic Ocean, where a fixed map-east direction is used to define wave spectral directions.

1. Introduction

The ice coverage in the Arctic Ocean shrunk as high as 86^{o} N in summer 2007, opening new shipping routes cross the Arctic and calling ocean surface wave models to extend at high latitudes. It seems to be only a matter of time before the whole Arctic Ocean has to be included in global ocean surface wave models. The major problem to extend a latitude-longitude (lat-lon) grid wave model at high latitudes is the diminishing longitude grid-length towards the Pole, which exerts a severe restriction on time steps of finite-difference schemes (advection and diffusion in particular). Another problem is the increased curvature of the parallels at high latitudes that renders the scalar assumption of a vector component defined relative to the local east direction invalid in the polar region and undefined at the Poles. In ocean surface wave models (WAMDI Group 1988, Booij et al 1999, Tolman et al. 2002), the wave energy spectrum is discretised into directional components relative to the local east. Each directional component is treated as a scalar, that is, the spectral component is transported into the corresponding one at the downstream grid point. This scalar assumption is a good approximation outside the polar region and is refined by a great-circle turning term as ocean wave travel along great circles. However, it becomes erroneous in the polar region since the change of direction over one longitude grid grows too large to be ignored on a reduced grid. For instance, if there are 8 grid cells in one circular row around the Pole, the local east direction changes 45º over one longitudinal grid. The scalar

Corresponding author address: Dr Jian-Guo Li, Met Office, FitzRoy Road, Exeter EX1 3PB, UK
Email: Jian-Guo.Li@metoffice.gov.uk *Tel.* +44 1392 884 885.

assumption of corresponding directional components in neighbouring cells are at the same direction is clearly no longer held here. The scalar assumption will be even more ridiculous for cross-pole transport, because its direction will be completely opposite to that of the corresponding component at the arrival cell across the Pole.

Among other grids developed to tackle the polar problems, the spherical multiple-cell (SMC) grid (Li 2011) is an efficient approach. The SMC grid has the flexibility to remove all land points out of the wave propagation schemes and requires minimal changes to the lat-lon grid finite-difference schemes because the lat-lon "rectangular" cells are retained. The SMC grid relaxes the Courant-Friedrichs-Lewy (CFL) restriction of the Eulerian advection time-step by merging longitudinal cells towards the Poles as in a reduced grid (Rasch 1994). Round polar cells are introduced to remove the polar singularity of the spherical coordinate system. Classic numerical tests have been used for validation of the SMC grid. A fixed reference direction, for instance, the map-east direction as viewed in a stereographic projection, is substituted for the local east direction in the Arctic to define the wave spectral components. This paper will show the implementation of the SMC grid in the Met Office global ocean surface wave model, which is adapted from the WAVEWATCH III model (Tolman et al 2002). Satellite altimeter and buoy wave observations are used for validation of the SMC grid wave model and comparison with the original lat-lon grid WAVEWATCH III model.

The unstructured feature of the SMC grid also allows refined resolutions near coastlines and small islands, while keeping the open ocean at coarse resolutions. This multi-resolution approach is operationally economical and resolving small islands is desirable for wave models because coastline blocking is an important sink of ocean surface waves (Tolman 2003, WISE Group 2007). Also in this paper an ocean wave spectral propagation test on a three-tiered multi-resolution SMC grid is used to demonstrate the coastline blocking and to test the map-east reference direction method.

2. Wave propagation equations on a sphere

Eulerian ocean surface wave model is based on a 2D spectral energy balance equation. In the 2-D spherical coordinates with longitude λ and latitude φ, the equation is given by

$$
\begin{aligned}
&\frac{\partial \psi}{\partial t} + \frac{\partial F_x}{\partial x} + \frac{\partial \left(F_y \cos\varphi\right)}{\cos\varphi \partial y} + \frac{\partial \left(\dot{k}\psi\right)}{\partial k} + \frac{\partial \left(\dot{\theta}\psi\right)}{\partial \theta} = S \\
&F_x \equiv \left(u + U_x\right)\psi - D_x \,\partial \psi / \partial x \\
&F_y \equiv \left(\upsilon + U_y\right)\psi - D_y \,\partial \psi / \partial y
\end{aligned}
\tag{1}
$$

where $\psi(t, \lambda, \varphi, k, \theta)$ is any component of the ocean surface wave energy spectrum, t is the time, k is the wave number, θ is the spectral direction usually defined from the local east direction, u and υ are the zonal and meridian wave propagation speed, U_x and U_y are the ambient current velocity components, D_x and D_y are the diffusion coefficients, and S the source term. The geophysical coordinates x and y are defined locally eastward along the parallel and northward along the meridian, respectively. So their increments are given by $dx = r\cos\varphi d\lambda$, $dy = rd\varphi$, where r is the radius of the sphere. The overhead dot indicates time differentiation along the wave propagation path. The r.h.s S represents all source terms. This study uses an adapted version of the WAVEWATCH III model (Tolman et al 2002) and its source terms are unchanged from the original model (Tolman and Chalikov 1996).

Note that Eq. (1) is equivalent to its Cartesian counterpart except that the meridian differential term involves an extra cosine factor which renders the term undefined (singular) at the Poles. Thus, except for at the Poles, the spherical wave energy balance equation (1) can be approximated using finite-difference schemes similar to those used in the Cartesian grid. The only difference between the Cartesian and spherical versions of these finite-difference schemes is that the latter has an extra cosine factor. Because the SMC grid retains the lat-lon grid cells, the wave energy balance equation (1) is also valid on the SMC grid (Li 2011).

a. Combined advection-diffusion term

The diffusion term in (1) may be considered as the sub-grid mixing term as in atmospheric models because the model wave spectrum represents the spatial average over one grid cell. This diffusion term is parameterised to alleviate the so called garden-sprinkler effect (GSE) due to discretisation of the wave energy spectrum (Booij and Holthuijsen 1987, Tolman 2002, Ardhuin and Herbers 2005). In this SMC grid wave model, the combined advection-diffusion term is estimated with an upstream non-oscillatory 2nd order (UNO2) advection scheme (Li 2008). Some wave models still use the efficient 1st order upstream scheme and rely on its implicit diffusion to smooth off the GSE (WAMDI 1988, Booij et al. 1999, Janssen 2008). However, the implicit diffusion of the 1st order upstream scheme is not up to the smoothing job because its diffusivity vanishes in the transverse direction if the wave direction is along one axial direction, causing unrealistically long shadows behind small islands (WISE Group 2007). Although shifting component directions out of alignment with axial directions may avoid the long shadows, it could not alter the inherent natures of the implicit diffusion, such as; its diffusivity varies with the Courant number. For regional models where long-distance propagation (and hence GSE smoothing) is not required, the 1st order upstream scheme is still a good choice. For global models it is considered too diffusive (Tolman 1992) in the propagation direction though its implicit diffusion is, sometimes, not enough for GSE smoothing. High order advection schemes then become the preferred choices for global wave models so that a 2nd order explicit diffusion term can be included for the GSE smoothing. It is also convenient to make the explicit diffusion term stronger in the transverse direction. The presence of the 2nd order explicit diffusion term, however, makes it unnecessary to use 3rd or higher order advection schemes in wave models because the diffusion term degrades all high order advection schemes to an equivalent 1st order scheme (Li 2008). Using a 2nd order advection scheme then becomes the most optimised choice to maintain efficiency and to include an explicit diffusion term as in (1) for the GSE smoothing. The UNO2 scheme has been used in the Met Office operational wave models since 2006. Its performance is comparable to that using a 3rd order scheme (Leonard 1991) but saves about 30% of advection computing.

Another feature of the SMC grid is the unification of boundary conditions with internal flux evaluations. Cell faces at coastlines are assumed to be bounded by two consecutive empty cells. Thus, any wave energy transported into these empty cells will disappear, and no wave energy will be injected out of these zero cells into any sea cells. This convenient setup conforms to the zero wave energy boundary condition at land points used by ocean surface wave models and allows all the boundary cell faces to be treated in the same way as internal faces. In addition, the periodic boundary condition for a global model is automatically included by the unstructured grid so there is no need to add extended columns as in the lat-lon grid. An additional benefit of using two consecutive zero-boundary cells beyond the coastline is the complete blocking of wave energy by single-point islands. On a conventional lat-lon grid, wave energy can ‘leak’ through a single-point island due to the interpolation with neighbouring sea points in transport schemes which use a 5-point stencil like the UNO2 scheme. In the SMC grid, any single-point island is extended with two zero cells beyond its boundary face. As a result, wave energy cannot pass through such ‘expanded island’. Sub-grid obstructions in WAVEWATCH III (Tolman et al 2002) follow the approach of Hardy et al (2000). This scheme is also implemented into the SMC grid propagation scheme with a simplified single transparency for each sea cell.

b. Refraction

Refraction is one primary physical process that affects surface wave propagation. Refraction formulations in contemporary surface wave models are based on the linear theory, assuming slow-varying ocean depth, which leads to the following surface wave dispersion relationship (Battjes 1968):

$$\omega^2 = gk\tanh(kh) \tag{2}$$

For a given intrinsic angular frequency ω, the wave number k varies with water depth h and can be determined by the following iteration algorithm, starting with $k_i = 1/h_g$:

$$k_{i+1} = 1/\left(h_g \tanh(hk_i)\right) \tag{3}$$

where i is the iteration number, $h_g = g/\omega^2$ will be referred to as the *gravity depth*. The gravity depth is a practical depth scale to define shallow and deep waters in relative to a given wave frequency.

Phillips (1977) derived the surface wave ray equation from the dispersion relationship (2) and the following kinematical conservation equation:

$$\partial\mathbf{k}/\partial t + \nabla(\omega + \mathbf{k}\cdot\mathbf{U}) = 0 \tag{4}$$

where $\mathbf{k} = (k\cos\theta,\ k\sin\theta)$ is the wave number vector, θ is the wave propagation angle measured from a reference direction (usually the local east), ∇ is the 2-D spatial gradient operator, and $\mathbf{U}$ is the ambient current velocity. Inserting the dispersion relationship (2) into (4), we have

$$\partial\mathbf{k}/\partial t + \left(c_g + U_k\right)\nabla k + \xi k\nabla h + k\nabla U_k = 0 \tag{5}$$

where $U_k = \mathbf{k} \cdot \mathbf{U} / k$ is the ambient current velocity component along the **k** direction, $\xi = \omega / \sinh(2kh)$ is a refraction factor, and c_g is the wave group speed defined as

$$c_g = \partial\omega/\partial k = c_{gd}\left(\tanh(kh) + kh/\cosh^2(kh)\right) \tag{6}$$

in which $c_{gd} = g/2\omega$ is the group speed in deep waters ($h >> h_g$). Surface wave energy is believed to travel at the group speed rather than the phase speed $c = \omega/k$. Note that the group speed is not a monotonic function of the water depth as shown in Fig.1. As waves move towards shallow waters, the group speed increases at first and reaches a maximum when the water depth decreases to the gravity depth h_g. The maximum speed is given by

$$c_{gm} = c_{gd}\beta_m, \qquad at \;\; h = h_g \tag{7}$$

where β_m ~ 1.19968 is the root of $\beta \tanh \beta = 1$. After the peak speed, wave group speed starts to decrease with water depth and can be approximated in shallow waters by

$$c_{gs} = \sqrt{gh}, \qquad if \quad h << h_g \tag{8}$$

Hence swells from deep waters will be 'stretched' or 'strained' around the gravity depth before the usually shoaling effect near coastlines. The 'stretched' wave height at the gravity depth is about 10% lower than that in deep waters because the peak speed is 1.2 times of the deep water speed. Note that the gravity depth is a function of wave frequency so shallowness is a relative description to surface waves. For wind waves, the frequency range is from about 0.05 to 0.5 Hz, which results in a gravity depth ranging from 100 to 1 m. So oceans over a few of hundreds meters in depth are considered deep for wind waves. For tsunami waves, however, the entire world oceans are shallow because tsunami frequency is extremely small. It can be worked out from Fig.1 that the group speed exceeds the deep water speed in the region from roughly $h_g/3$ to $3h_g$. So it would be practical to say that, for a given surface wave frequency, the water is deep if $h > 3h_g$ or shallow if $h < h_g/3$. This shallow or deep water definition is more tangible than the conventional definition kh << 1 or >> 1.

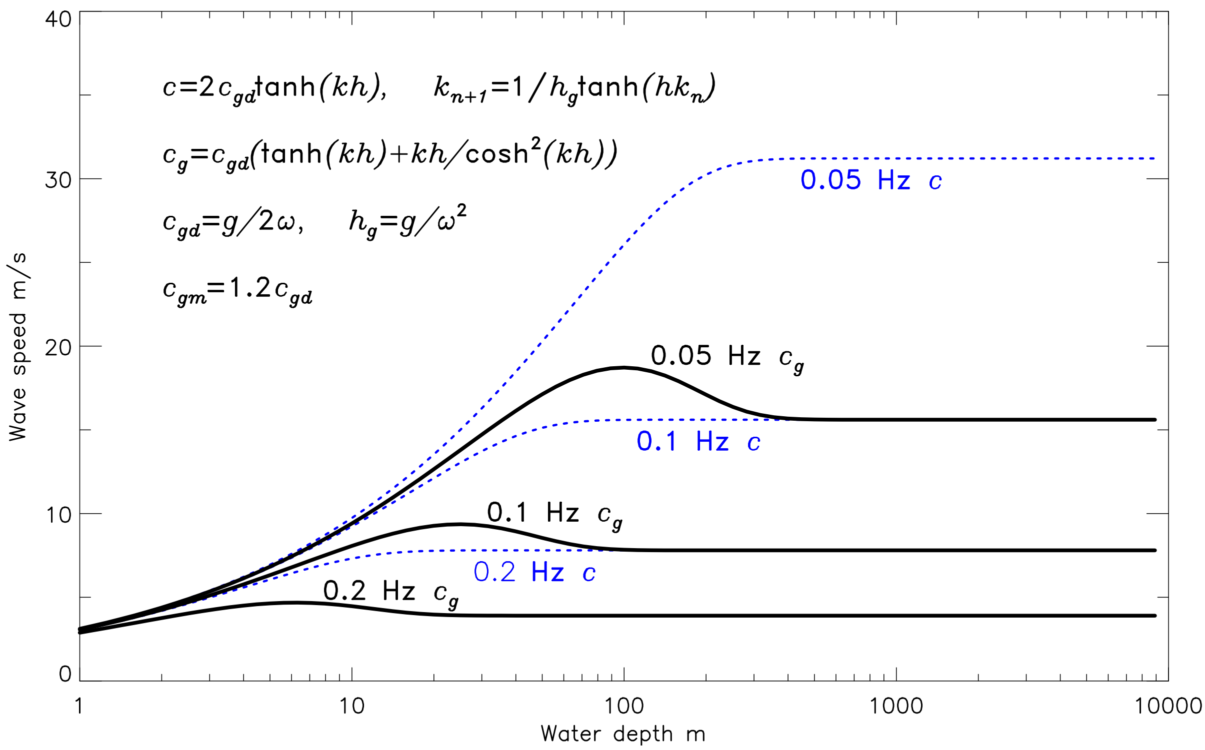

Fig.1. Variations of ocean surface wave speed with water depth.

Phillips (1977) assumed steady wave train ($\partial \mathbf{k}/\partial t = 0$) to derive the following ray equations from (5):

$$\left(c_g + U_k\right)\partial k/\partial s = -\xi \mathbf{k} \cdot \nabla h - \mathbf{k} \cdot \nabla U_k \tag{9a}$$
$$\left(c_g + U_k\right)\partial \theta/\partial s = -\xi \mathbf{n} \cdot \nabla h - \mathbf{n} \cdot \nabla U_k \tag{9b}$$

where s is the distance along the wave path at the **k** or θ direction and **n** = (-sinθ, cosθ) is a unit vector normal to the **k** direction to the left or at θ + π/2. Note that the wave energy travelled distance in one time step Δt, at the **k** direction in the presence of an ambient current, is $\Delta s = (c_g + U_k)\ \Delta t$, so the time changing rate of the wave number along the wave path is given by inserting Δs into (9a)

$$\dot{k} = -\xi \mathbf{k} \cdot \nabla h - \mathbf{k} \cdot \nabla U_k \tag{10}$$

And the θ changing or refraction rate along the wave path is given by inserting Δs into (9b)

$$\dot{\theta}_{rfr} = -\xi \mathbf{n} \cdot \nabla h - \mathbf{n} \cdot \nabla U_k \tag{11}$$

This refraction rate can also be derived in analogous to the Snell's law in geometrical optics (e.g. Longuet-Higgins 1956, Kinsman 1965 and Holthuijsen et al 2003) and is often referred to as the geometrical optics refraction rate. The simplicity of the optical refraction theory makes it ideal for operational models. Magne et al. (2007) compared a simple optical refraction model and some more complicated models with observations in step ocean canyons, near San Diego, California and concluded that the simple refraction model is in good agreement with observations and very robust even over wide range of depth gradients.

It is worth pointing out that that the above refraction theory is based on the spatial gradient of the wave phase speed. But ocean surface wave energy is transported at the group speed (6). If the group speed is substituted for the phase speed in the Snell's law, the wave refraction rate can be rewritten as:

$$\dot{\theta}_{rfrg} = -\mathbf{n} \cdot \nabla\left(c_g + U_k\right) = -\zeta \mathbf{n} \cdot \nabla h - \mathbf{n} \cdot \nabla U_k \tag{12}$$

which is identical to the phase speed refraction rate (11) except for a new refraction factor, $\zeta = 2\omega(1 - h/h_g)/\left(2kh + \sinh(2kh)\right)$. These two refraction rates (11 and 12) do not make much difference near shore ($h << h_g$) as phase speed and group speed merge asymptotically with diminishing water depth. The difference is not prominent in the deep water ($h >> h_g$) where both refraction rates vanish with increased water depth. Only in the intermediate water of depth close to the gravity depth ($h \sim h_g$), the two refraction rates differ slightly.

If the group speed rate (12) is used, deep water waves approaching shallow water would first be deviated from the depth gradient direction until h approaches h_g. The refraction is reverted towards the depth gradient direction after h becomes smaller than h_g. According to the phase speed refraction rate (11), however, the surface waves will be bent towards the depth gradient direction all the way from deep water to the shoreline. This subtle difference is difficult to tell in global wave models due to poor resolution of coastal bathymetry and the fact that refracted waves die shortly when they reach the shoreline along with all refraction effects. High resolution coastal wave models might be able to simulate the difference and matching high resolution observations are required for verification. This is, however, beyond the scope of this study. The observation data density around the gravity depth area in the Magne et al. (2007) study is not enough for this verification.

It should be emphasized that the linear refraction theory is only valid when the water depth is non-zero. When h approaches zero, both refraction rates becomes undefined because both the ξ and ζ factors approach a common infinitive value, $0.5\sqrt{g/h}$. It is then a customary in wave models to use a minimum water depth for refraction term. If the minimum water depth is 10 m, the refraction factors will be less than 0.5 at the largest.

Apart from shallow water depth, steep ocean floor and large time step may also result in a large refraction rate. For instance, if the discrete depth gradient is assumed to be $\Delta h/\Delta x = 0.1$ and time step is $\Delta t = 1000$ s, the maximum refraction angle per time step might be $\Delta t\Delta h/2\Delta x \sim 50$ rad or about 8 full circles, which is too large to fit into any advection-like refraction schemes used in contemporary wave models. One way to avoid this unrealistic large refraction increment is to use small time step but this usually turns out to be too restrictive for wave models. Since refraction in wave model is usually a minor process and is confined to coastal regions, the refraction increment is simply reduced to fit for the advection-like CFL condition in some wave models (WAMDI group, 1988, Booij et al 1999 and Tolman et al 2002). The CFL condition requires the refraction angle increment per time step to be less than the directional width (about 10º) and, of course, reduces the refraction effect. Here for the SMC grid wave model, a rotation scheme is substituted for the advection-like scheme to estimate the refraction term so that the CFL limit can be avoided. The rotation scheme is similar to the re-mapping scheme used for advection term and is unconditionally stable.

Although the rotation scheme does not have any limit on the refraction increment, the refraction angle should not pass beyond the depth gradient line (where $\mathbf{n} \cdot \nabla h = 0$) as stated in the refraction rates (11) and (12). This imposes a physical limiter on the total refraction angle. To avoid refraction rotation beyond this physical limiter, the angle between the spectral direction and the depth decrease direction is calculated first by:

$$\alpha = \cos^{-1}\left[-\left(h_x \cos\theta + h_y \sin\theta\right) \Big/ \sqrt{h_x^2 + h_y^2}\,\right] \tag{13}$$

Because FORTRAN function ACOS returns value between 0 and π, the maximum refraction angle (absolute value) is then chosen to be less than π/2 with $\Delta\theta_{mxrfr} = \eta \min(\alpha, \pi - \alpha)$. The scaling factor η (< 1) is introduced to prevent all waves from being refracted into the depth gradient direction within one time step, which may cause numerical instability like caustics in ray tracing models (Cavaleri and Malanotte-Rizzoli 1981, Ardhuin et al 2001). This scaling factor also creates some space for merging the refraction with other direction changing terms, such as the refraction by ambient current.

c. Great circle turning

Wave energy is believed to travel along the shortest route on the ocean surface, that is, along great circles on the sphere. So wave spectral component at a slant direction will not be confined at the direction but shift gradually with latitude along its great circle path, a procedure known as the great circle turning (GCT). Like refraction, the GCT term also contributes to wave direction change. Assuming the great circle direction is at θ from the local east at latitude φ, the following cosine product of these two angles is conserved on the great circle path:

$$\cos\theta \cos\varphi = \cos\theta_0 \cos\varphi_0 \tag{14}$$

This provides a simple rule for navigation along great circles and leads to the following GCT rate

$$\dot{\theta}_{gct} = -\left(c_g / r\right)\cos\theta \tan\varphi \tag{15}$$

where the over-dot indicates time differentiation along the great circle path. Because of the large value of the earth's radius $r = 6.37\text{x}10^6$ m, the wave energy angular speed, c_g/r, is on the order of 10^{-6} rad s^{-1}. For time step less than 15 min, the GCT angle will be less than 1° per time step below 85° latitude. Considering the directional width is about 10º, the GCT term will usually fit for an 'advection-like' scheme. However, as the refraction term is calculated with a rotation scheme in the SMC grid model, the GCT term is simply appended to the refraction term to form a total rotation angle. The rotation subroutine rotates each directional component by their combined rotation angle and portions its energy into the two directional components which the rotated one covers after the rotation. This simple rotation subroutine not only removes the time step restriction on the refraction angle but also adds an implicit diffusion in the θ direction because its implicit diffusivity is equivalent to that of the 1st-order upstream scheme. This additional smoothing in the transverse direction is desirable for wave models to mitigate the GSE.

d. Wave spectral reference direction

Ocean surface wave energy spectrum is usually defined as discrete directional components from a reference direction at the local east and each directional component is assumed to be a scalar in wave propagation, that is, the component is transported into the corresponding one in the downstream cell. This scalar assumption is a good approximation for global wave model when the ice covered Arctic area is excluded and is refined by the GCT term. However, the scalar assumption becomes erroneous at high latitudes since the change of direction grows too large to be ignored if a reduced grid is used. Besides, the north polar cell does not have a local east direction as all direction from there is southward. The invalid scalar assumption based on local east reference direction in the polar region prevents extension of ocean surface wave models at high latitudes in response to the retreating of the Arctic sea ice.

This invalid scalar assumption problem in the reduced grid polar region can be avoided by switching to a fixed reference direction, for instance, the map-east direction as viewed on a stereographic projection of the polar region. Assuming the angle from the map-east to the local east is α, the wave spectral component for a given direction of angle θ from the local east will have an angle θ′ = θ + α from the map-east. Its zonal and meridian transport velocity components are then given by

$$\begin{aligned} u &= c_g \cos\theta = c_g \cos(\theta' - \alpha) \\ \upsilon &= c_g \sin\theta = c_g \sin(\theta' - \alpha) \end{aligned} \qquad (16)$$

Note that the polar cell does not have a local east direction so the velocity could not be defined at the Pole as zonal and meridian components. In the SMC grid propagation scheme, however, only the meridian velocity component at the edge of the polar cell is required and there is no need to define the velocity at the polar cell centre (Li 2011). This is one of the advantages to use a polar cell centred at the Pole. Because a given direction θ′ from the map-east is constant in the Arctic region, the spectral component in the map-east system can be treated as a scalar for transport in the polar region.

This map-east direction can be conveniently approximated with a rotated grid with its rotated pole on the Equator. The standard polar region becomes part of the 'tropic region' in the rotated grid so the longitudinal direction of the rotated grid can be substituted for the map-east direction. For instance, if the rotated pole is at 180ºE on the Equator, the angle α from this map-east to the local east at longitude λ and latitude φ within the Arctic region can be worked out with:

$$\alpha = \mathrm{sgn}(\cos\varphi \sin\lambda) \arccos\left[\frac{\cos\lambda \sin\varphi}{\sqrt{1-(\cos\lambda\cos\varphi)^2}}\right] \qquad (17)$$

If the map-east is used within the Arctic region and local east in the rest of the model domain for definition of the wave spectrum, there will be no fixed corresponding components between the two systems because α varies with longitude and latitude. For this reason, wave spectra defined by local east could not be mixed up with those defined from the map-east and the Arctic region using the map-east reference direction has to be separated from the rest which uses the local east reference direction. In the SMC grid, the Arctic part and the rest (will be referred to as the *global part*) are linked together through 4 over-lapping rows. Wave spectra in the lower two of the 4 over-lapping rows in the Arctic part are updated with wave spectra from the global part after they are rotated anticlockwise by α. Wave spectra in the upper two rows of the 4 over-lapping rows in the global part are updated with wave spectra from the Arctic part after a clockwise rotation by α. Because of the unstructured nature of the SMC grid, the overlapping cells are treated as other cells and the propagation are calculated together for both parts.

3. Comparison with a lat-lon grid model

The WAVEWATCH III wave model is adapted for this comparison. The lat-lon grid version is set at the resolution of $\Delta\lambda$ = 360º/1024 = 0.3515625º and $\Delta\varphi$ = 180º/768 = 0.234375º, identical to the horizontal grid of the Met Office weather forecast model, which provides the marine surface wind. This lat-lon grid wave model will be referred to as the global 25km (G25) model as the latitudinal grid length is about 25 km. The SMC grid is implemented into this model with a new compiling option. For comparison purpose, the SMC grid is set to be identical to the G25 grid except that the SMC grid merges cells at high latitudes and removes cells on land, resulting in a total cell number of 429,722, only about 55% of the full lat-lon grid (1024x768). This SMC grid wave model will be referred to as the SMC25 model and the Arctic of this SMC25 grid is shown in Fig.2. The two filled rings (at about 82-83ºN) indicate the first and the last overlapping rows. They can be viewed as the outmost row for the Arctic part and the north-most row of the global part, respectively. Due to the polar restriction of the lat-lon grid, the Arctic part above 83ºN is not included in the G25 model. This, however, does not affect the two model comparison as this polar region is covered by sea ice so the Arctic part in the SMC25 model is effectively not used. The global part of SMC25 model matches with the G25 model except for the cell-merging at high latitudes. Both models are forced with the same 25km wind from the Met Office atmospheric model. Ocean current is not included in both the G25 and SMC25 models for this comparison. Nevertheless, current influence on waves, including its refraction effect, is quite limited even in the Gulf Streams (Holthuijsen and Tolman 1991) or in a river mouth (Guan et al 1999).

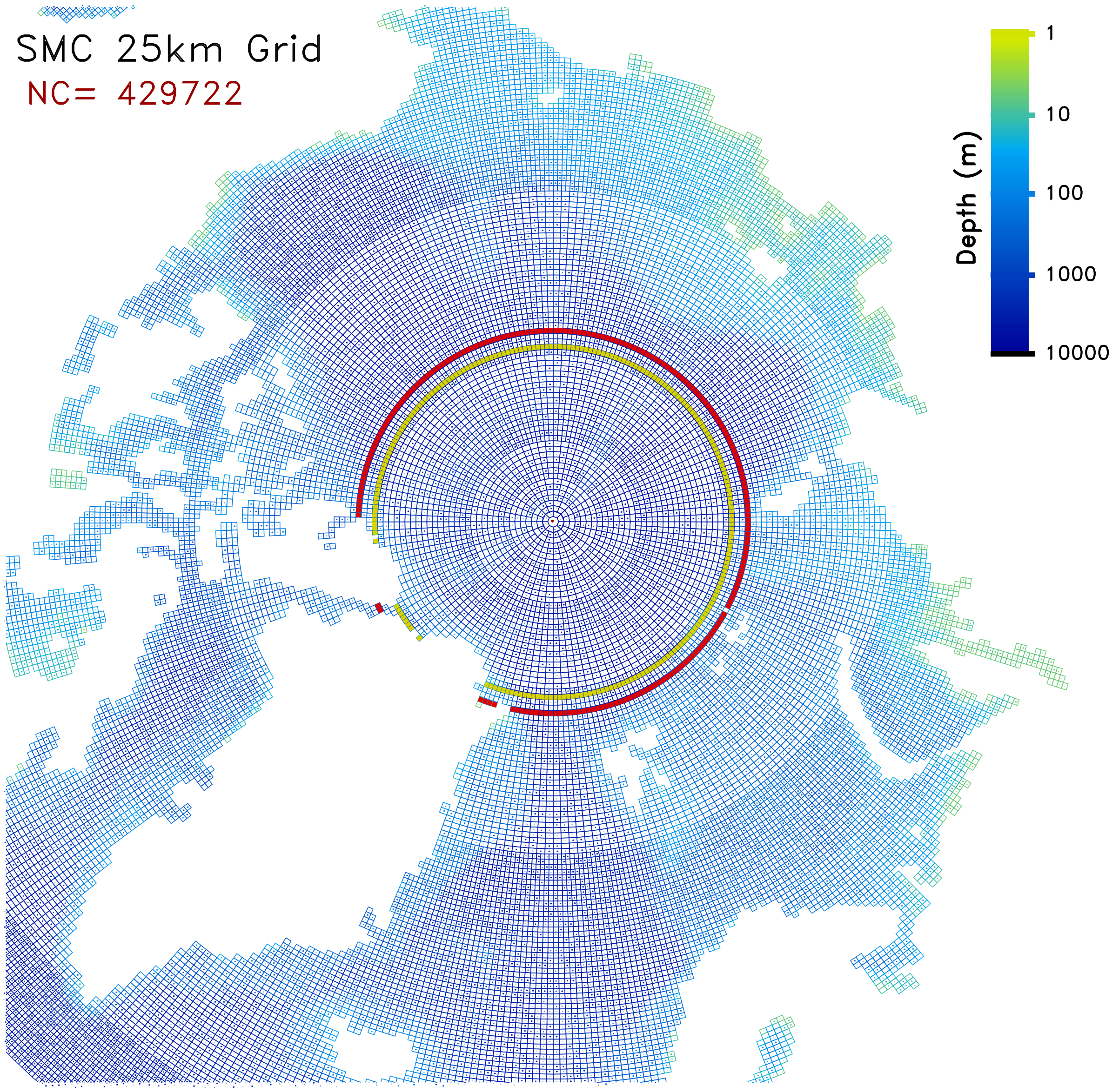

Fig.2. The Arctic part of the global 25km spherical multiple-cell grid.

Both the G25 and the SMC25 wave models are validated with the significant wave heights (SWHs) from the radar altimeter 2 (RA2) on board the European Space Agency (ESA) Envisat satellite and buoy wave spectra from the US National Data Buoy Centre (NDBC). The study period covers over 3 months from 20 July 2010 to 31 October 2010 and the one month, September 2010, is used for comparison with altimeter and buoy data. September coincides with the annual minimum of Arctic sea ice coverage and allows the open sea latitudes as high as possible. The satellite SWHs are collocated with interpolated model values to minimise modification of the satellite data. This allows more filters to be applied on the satellite data if required. For instance, spurious large satellite SWHs near coastlines can be filtered out by comparing to the interpolated model values (Li and Holt 2009). These large coastal SWHs are difficult to remove with normal satellite data filters. Averaging the satellite data within model grid cell would make this kind of filter impractical.

Fig.3 shows the SMC25 model SWH field on 2 September 2010 when the sea ice coverage in the Arctic is close to its annual minimum. The highest latitude of the Arctic sea ice edge reached about 83ºN in 2010, just at the north boundary of the G25 model and the north edge of the SMC25 global part. The Arctic part of the SMC25 model is virtually unused because they are covered by sea ice. The global part of the SMC25 model covers exactly the same area as the G25 grid and is used for the comparison.

The spectral performance of the wave model is assessed with a 4-bin sub-range wave height (SRWH), which is defined in analogue to the SWH but integrated over a limited frequency range (Li and Holt 2009). The 4-bin margins are marked with wave period T > 16 s, 16-10 s, 10-5 s and T < 5 s, respectively.

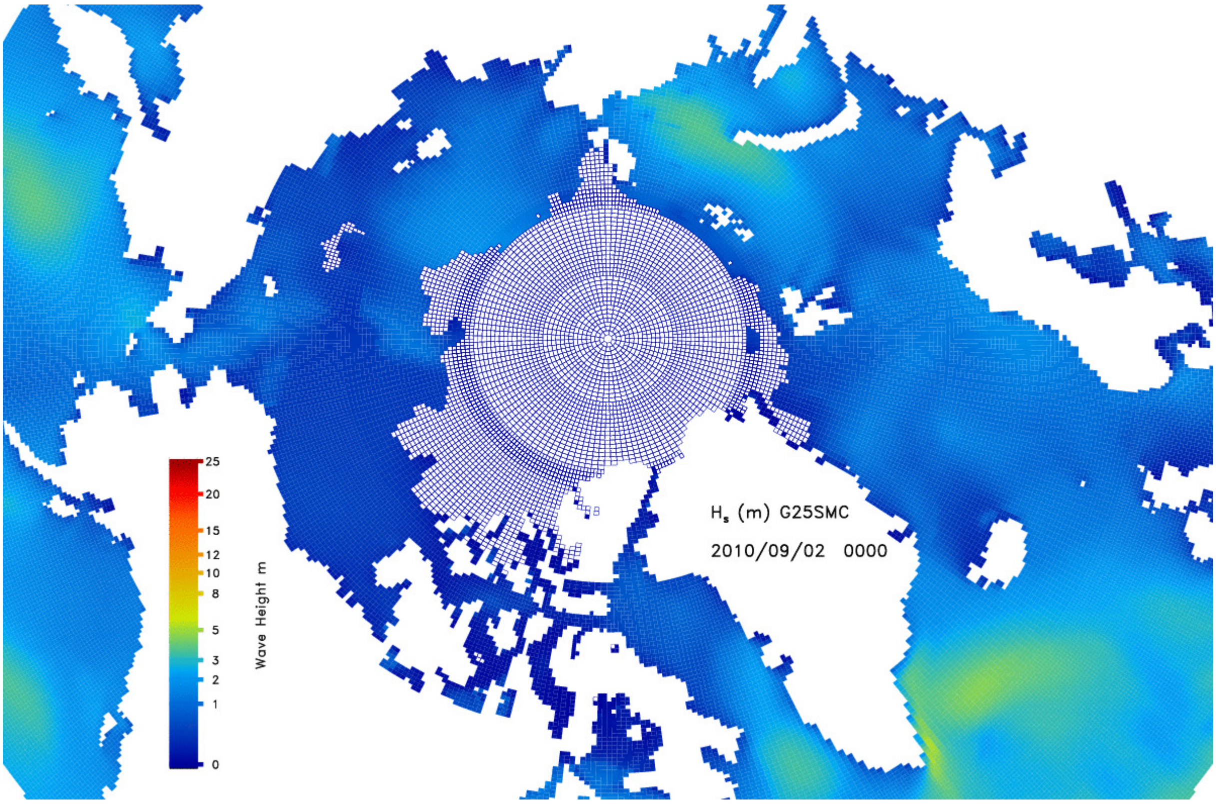

Fig.3. SMC25 model SWH field in the Arctic on 2 September 2010, revealing the annual minimum ice cover.

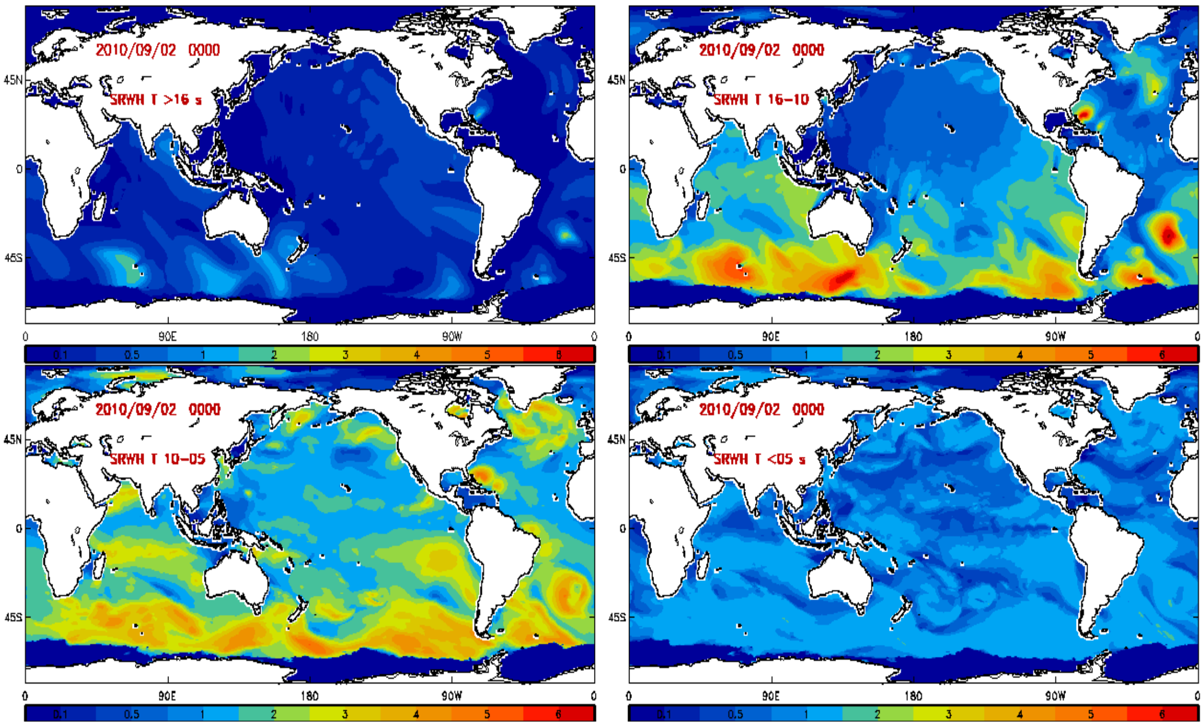

Fig.4. SMC25 model 4-bin SRWH field on 2 September 2010.

Fig.4 shows the 4-bin SRWH field from the SMC25 model on the same day as Fig.3. The T > 16 s bin SRWH represents the long-wave or the swell. Note that the disintegrated swell field in the north Pacific is primarily the results of blocking by the Pacific islands. The T < 5 s bin is pure wind sea and is hardly affected by the propagation schemes. The other two bins (16-10 and 10-5 s) are mixtures of swell and wind sea and they show some propagation effect as well, such as the shadows of island-blocking in the 16-10 s bin. Hence, the propagation effect can be examined visually with movies of the first two bins without the interfering wind sea.

Fig.5 shows a comparison plot of the model and altimeter SWH along a satellite track on 17 September 2010 (top panel). The two model SWH values (red for G25 and green for SMC25) are in quite good agreement. This track is particularly selected to show a case when the model wind speed (lower panel) failed to catch a storm peak in the North Pacific, resulting in underestimation of the wind sea field in both wave models. So it represents nearly the worst case of discrepancy between the model and the satellite. Note that this track also has a section in the Arctic and this section reveals the good agreement of the three data sets in the Arctic despite of the reduced spatial resolution of the SMC25 model.

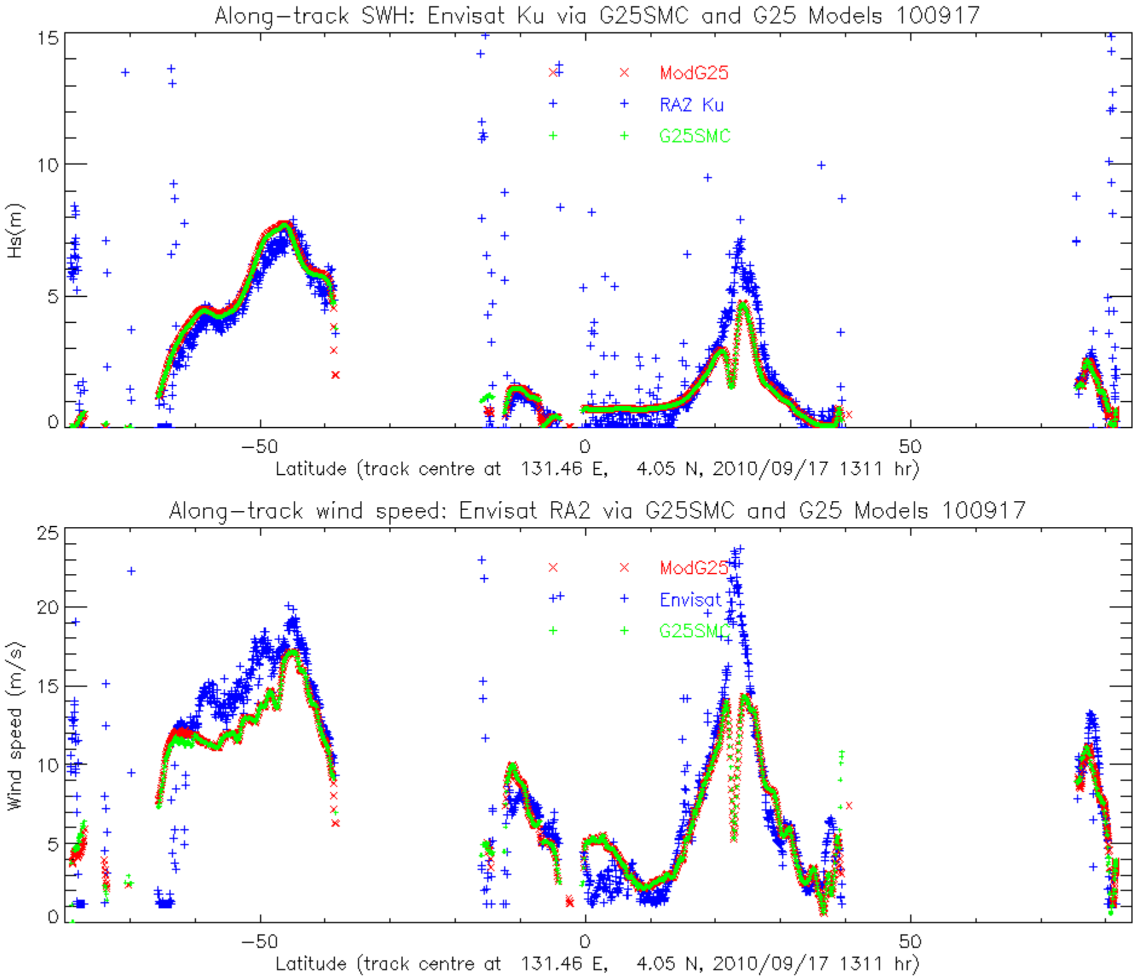

Fig.5. A typical comparison of model and altimeter SWH along a satellite track.

To quantify the comparison of the two models, the collocated model and satellite data over one month (September 2010) are packed into one scatter plot for each model and the validation results for the G25 and SMC25 models are shown side-by-side for comparison. Fig.6a shows the scatter plot of the collocated G25 model and altimeter SWHs. Fig.6b is the scatter plot of the SMC25 model. Apart from the standard filters recommend by ESA, an extra filter (RA2_SWH – Model_SWH < 4.0 m) is used to remove spurious coastal altimeter data. This is why there are no scattered points in the lower-right corners. The correlation coefficients are 0.933 and 0.931 for the G25 and SMC25 models, respectively. The root-mean-square (rms) error is 0.542 m for the G25 and 0.553 m for the SMC25. The increased rms error in the SMC25 model is attributed to the increase of coastal points in the collocated data. This is confirmed by the total number of collocated entries for the two models. The SMC25 model has 15,848 more collocated entries (total 707,419) than the G25 model (total 691,571). These extra entries must come from coastal regions as inner ocean satellite data points are the same for both models. Because altimeter SWHs are spuriously too large in coastal regions due to radar echo contaminations by land surfaces, the extra 15,848 coastal points would cause the rms to increase. This is confirmed by the increased altimeter mean (2.595 m) for the SMC25 collocated data, comparing with 2.572 m for G25. In fact, the SMC25 model mean (2.675 m) is closer to the altimeter mean than that of the G25 model (2.701 m). The increased temporal truncation error due to increased time step (from 180 s for the G25 model to 600 s for the SMC25 model) and reduced spatial resolution at high latitude due to cell merging in the SMC grid are also possible reasons for the increased rms error. This small increase in error is worth the large reduction in computing cost, which will be discussed later.

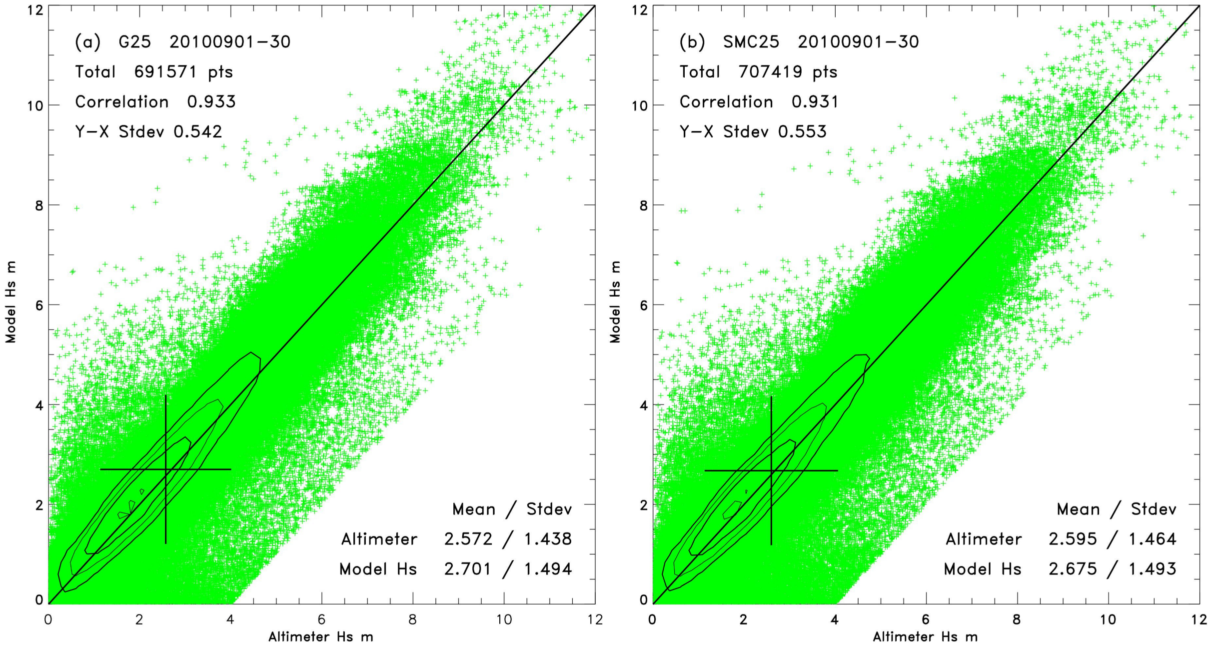

Fig.6. Comparison of G25 (a) and SMC25 (b) wave model SWH with September 2010 altimeter data.

Fig.7 shows the two model SWH comparison against 31 spectral buoys as listed in Table 1. Fig.7a is for the G25 and Fig.7b for the SMC25. The buoy results are consistent with those of the altimeter data comparison. The G25 model is slightly better than the SMC25 with slightly larger correlation coefficient (0.917 against 0.916) and smaller rms error (0.320 m against 0.321 m). So both the altimeter and buoy SWH comparison indicate that the SMC25 model is comparable to the G25 model in ocean surface wave height prediction.

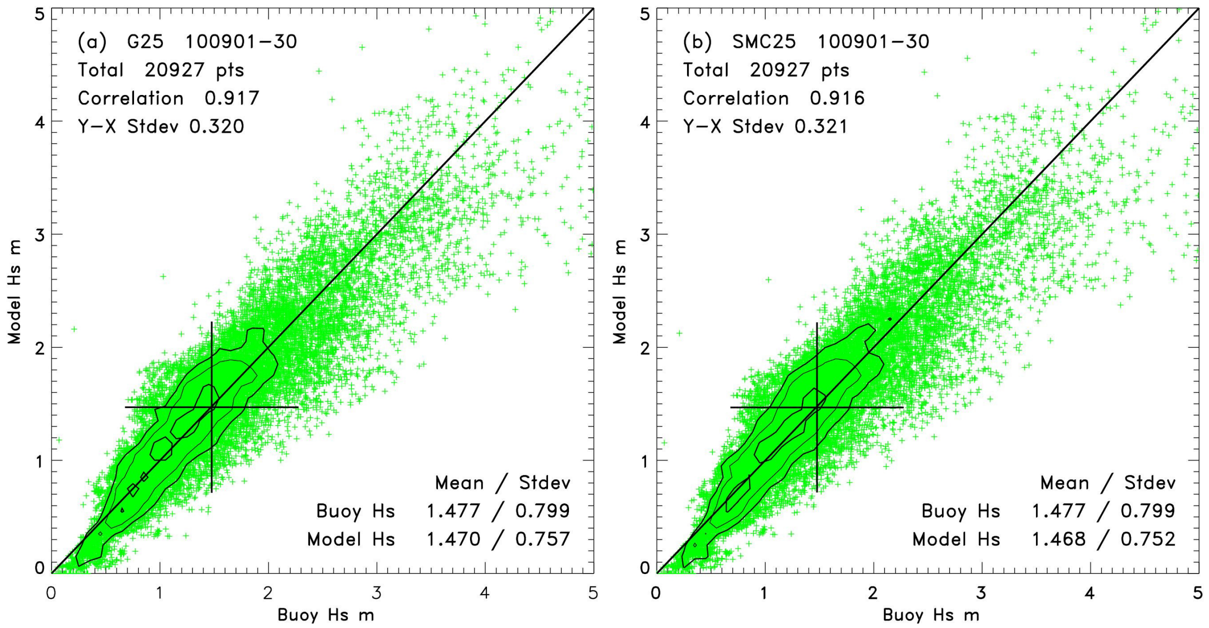

Fig.7. Comparison of G25 (a) and SMC25 (b) wave model SWH with September 2010 buoy data.

The spectral performance of the wave model is assessed by the 4-bin SRWH comparison with the 31 spectral buoys in Fig.8. The 4 panels in the left column are the scatter plots of the G25 model 4-bin SRWH against that of the 31 buoys and the right column are for the SMC25. The T < 5 s bin may be considered to be locally generated wind sea and independent of transport. As the two models use exactly the same source terms, the wind sea is identical. The T > 16 s bin may be considered to be the long-distance swell field. The two models also generated very similar results in this bin, indicating that the SMC25 propagation schemes are comparable to those in the G25 model. The other two bins (16-10 s and 10-5 s) are mixture of wind sea and swell fields. Performances of the two models are also comparable in these two spectral ranges, with G25 model slightly better in the 16-10 s bin and SMC25 slightly better in the 10-5 s bin.

Table 1. Spectral buoys used in the wave model validation.

Buoy_ID	*Latitude*	*Longitude*	44008	40.502°N	69.247°W	46028	35.741°N	121.884°W
41012	30.041°N	80.533°W	44014	36.611°N	74.836°W	46029	46.144°N	124.510°W
41013	33.436°N	77.743°W	44018	41.255°N	69.305°W	46042	36.789°N	122.404°W
41047	27.469°N	71.491°W	44025	40.250°N	73.166°W	46047	32.433°N	119.533°W
42002	25.790°N	93.666°W	44065	40.369°N	73.703°W	46050	44.641°N	124.500°W
42012	30.065°N	87.555°W	46011	34.868°N	120.857°W	46053	34.248°N	119.841°W
42020	26.966°N	96.695°W	46013	38.242°N	123.301°W	46086	32.491°N	118.034°W
42035	29.232°N	94.413°W	46015	42.747°N	124.823°W	51000	23.546°N	154.056°W
42036	28.500°N	84.517°W	46025	33.739°N	119.056°W	51100	23.558°N	153.900°W
42055	22.017°N	94.046°W	46026	37.759°N	122.833°W	51101	24.321°N	162.058°W
42056	19.874°N	85.059°W	46027	41.850°N	124.381°W			

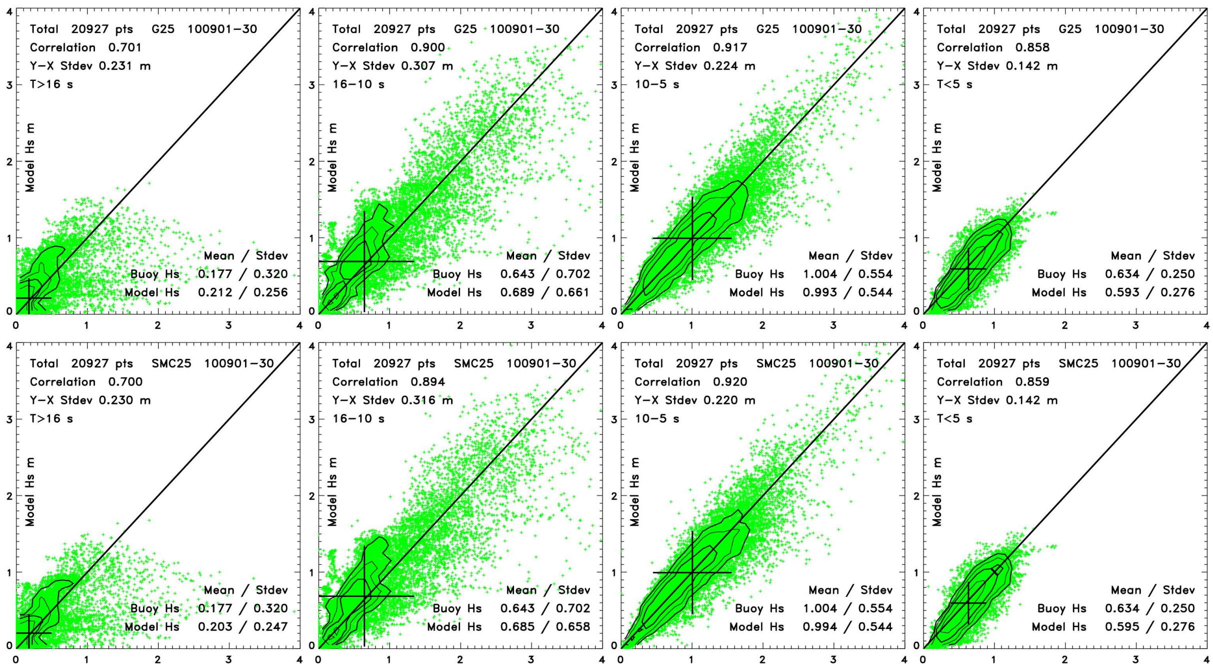

Fig.8. Comparison of G25 and SMC25 wave model 4-bin SRWH with September 2010 spectral buoy data.

The two refraction rates (11 and 12) are tested in the SMC25 model and their model results are compared with altimeter and buoy data, respectively. The results, as listed in Table 2, reveal some minor difference, with the phase speed refraction rate (11) on the better side. However, the coarse spatial resolution of the SMC25 grid is not enough to tell the subtle difference around the gravity depth and hence these comparisons can not be used to judge the two refraction rates. The results are provided here to show the magnitude of their influence on global ocean surface wave propagation. Higher model resolution near the coastlines and more observations in the stretching zone around the gravity depth than the present comparison are required to assess these two refraction rates. This is, however, beyond the reach of this study.

Table 2. Comparison of the group speed and phase speed refraction schemes.

	Group speed refraction rate (12)		Phase speed refraction rate (11)	
	Correlation	Diff RMS (m)	Correlation	Diff RMS (m)
RA2 SWH	0.930	0.556	0.931	0.553
Buoy SWH	0.915	0.325	0.916	0.321
SRWH T > 16 s	0.699	0.231	0.700	0.230

SRWH 10 – 16 s	0.895	0.317	0.894	0.318
SRWH 5 – 10 s	0.914	0.229	0.920	0.220
SRWH T < 5 s	0.859	0.142	0.859	0.142

The major advantage to use the SMC grid is that all land points have been removed out of the propagation schemes. Because the propagation schemes on the SMC grid are virtually identical to those in the lat-lon grid, removing 45% grid points implies roughly 45% reduction per time step in wave propagation computation. The merged cells at high latitudes allow the time step to be as large as 4 times of that in the lat-lon grid model, resulting in the actual calculation reduced further by a quarter. The combined CPU time reduction is more than 80% for the wave propagation on the SMC grid. The source terms are applied on sea points only at main time steps and are not affected by the grid change as both the G25 and SMC25 grid models share the same main time step, 1800 s. Assume the CPU time for the G25 model is P + S + W, where P and S represents the CPU times for the propagation and source terms, respectively, and W represents the start-up and write-out time, the CPU time for the SMC25 model can be estimated to be 0.2P + S + W.

In this comparison study the actual propagation time step is 180 s for the G25 model and 600 s for the SMC25, not exactly 4 times, because it has to be an integer factor of the main time step (1800 s). The models are run on the IBM Power 6 supercomputer in two configurations, a 1-day hind-cast run using 1 node (32 CPUs or 64 cores) and a 5.5-day forecast run on 4 nodes (128 CPUs). Table 3 list the average CPU times recorded by the 1-day and 5.5-day runs for the two models. The SMC25 model uses only about 64% of the G25 model CPU time in the 1-day 1-node runs. The percentage is increased to 69% for the 5.5-day 4-node runs. This increase reveals the non-linear scaling feature of the wave model parallelisation. The most probable cause is the delay by write-out from a single processor. The more the processors are used the more the time is wasted in the waiting. These timing tests indicate that the SMC grid can reduce the overall CPU consumption of the global wave model by about 1/3 in comparison with the original lat-lon grid. This huge reduction in computation cost is highly desirable for operational models and creates room for spatial resolution upgrade.

Table 3. Comparison of CPU times of the lat-lon and SMC grid models.

	G25 Lat-lon	SMC grid
Full grid points	1024x688	430581 (55%)
Advection time step	180 s	600 s
1-day on 1-node 32 PEs	330 s/task	210 s/task (64%)
5.5-day on 4-nodes 128 PEs	1800 s/task	1240 s/task (69%)

4. Wave propagation on a multi-resolution SMC grid

Unresolved small islands are the major source of errors in global ocean surface wave models as they are important sinks of the ocean surface wave energy (Tolman 2003). Missed island groups in coarse resolution global models lead to a persistent under-prediction of the blocking of wave energy (WISE Group 2007). Although the errors can be alleviated with sub-grid obstructions in the far fields, high resolution around islands is still the most appropriate approach for accurate swell prediction close to islands (Chawla and Tolman 2008). Near-shore bathymetry features are also attributed to some non-linear wave features, like freak waves (Janssen 2004). One feature of the unstructured SMC grid is that it can handle multiple resolutions and this is particularly useful to resolve small islands and detailed coastlines. As increasing resolution throughout the full model domain to resolve islands is not economical for operational models, using refined resolution near coastlines and around small islands with the SMC grid is then a very appealing option.

For demonstration purpose, a global 3-tiered (6 – 12 – 25 km) SMC grid is constructed and will be referred to as the SMC6-25 grid. An idealised wave propagation test is carried out on the SMC6-25 grid to illustrate the small islands blocking of ocean surface waves and the proposed map-east reference direction in the Arctic region, which could not be tested in the wave models against observations because of the sea ice coverage. Fig.9 shows the Hawaii Islands resolved in the SMC6-25 grid and compared with an image from a NASA satellite. All the 8 main islands visible in the satellite image are resolved in the SMC6-25 grid.

The idealised wave propagation test includes all the 4 terms (advection, diffusion, refraction and GCT) in (1) but does not have any source terms. The transient zone from the global to the Arctic parts is set from about 83 to 84ºN and the map-east reference direction is used within the Arctic part. Wave spectra are discretised with 36 directions but only one frequency at 0.0625 Hz or period T = 16 s. The initial spectra are assumed to be zero except cells in two belts between 52^{o} and 60^{o} latitudes. There is also a round patch of non-zero cells above 86^{o}N in the Arctic to test the transfer from the map-east to the local east reference directions. Another round patch of the same size as the Arctic one is initialised in the Atlantic close to the Equator. This will facilitate a simple comparison of the map-east direction method. The non-zero cells are assigned with a typical wind-sea spectrum defined by

$$E(\theta) = \begin{cases} E_0 \cos^2(\theta - \theta_p), & for\ |\theta - \theta_p| < \pi/2 \\ 0, & Otherwise \end{cases} \tag{18}$$

where $E_0 = 50/\pi$ is a constant, θ_p is the peak direction. The transported spectrum is integrated as the wave height, $H = \sqrt{\int E d\theta}$, similar to the SWH used in wave models apart from a constant factor.

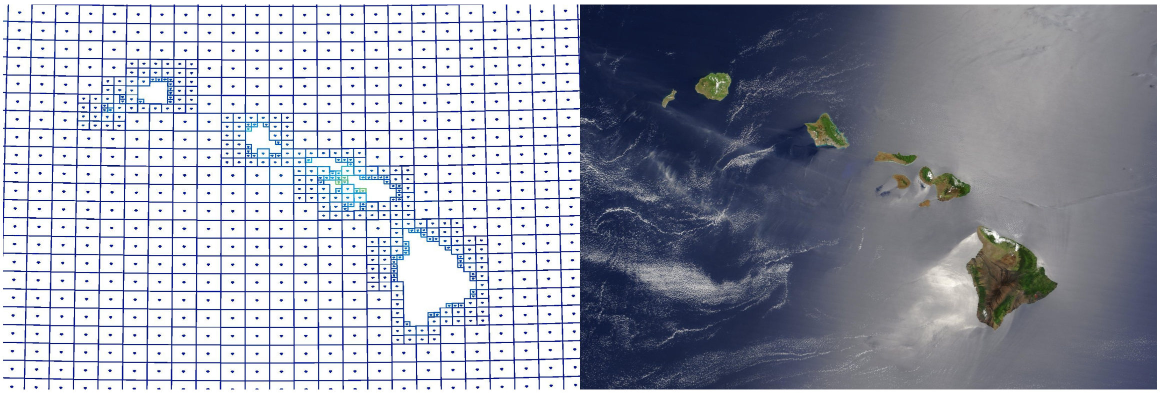

Fig.9 Comparison of the Hawaii Islands resolved in a SMC 6-25km grid and viewed by a satellite.

The initial wave height field is shown in the row (a) of Fig.10 and its non-zero wave height is constant 5 units. Note the wind-sea spectrum (18) has a peak direction θ_p from its reference direction. The peak direction is set to be 45° towards the northeast for the two round patches and the southern belt as indicated by the spectral roses in Fig.10. For the northern belt the peak direction is at -45° towards the southeast. Because the Arctic and global parts use different reference directions, the peak direction of the initial spectrum varies with longitude in the global part. Inside the Arctic part, however, the reference direction is fixed at the map-east so the initial spectral peak direction is constant for all non-zero cells there. This is why the initial Atlantic round patch is placed near the Equator where the direction has the minimum change rate with longitude.

The gravity depth is about 64 m for the given frequency (0.0625 Hz) and its deep water group speed is about 12.5 m s^{-1}. Multiple sub-time steps are used to satisfy the CFL requirements for different tiers of cells. The minimum time step is 300 s for the smallest cells (6 km), resulting in a maximum Courant number of 0.929. The unstructured pointers in the SMC code allow regrouping of cells so that cells of different sizes are separated into different time step (nested) loops for optimization.

The middle row (b) of Fig.10 shows the idealised wave propagation result after 40 hrs. The initial waves have travelled about 1800 km and typical wave propagation features are revealed. The Arctic patch is almost out of the Arctic part and shows a similar distribution as the Atlantic patch. The northern belt in the Atlantic has passed the British Isles and reached the Canary Islands. The blocking effects of the Azores islands are clearly illustrated. The northern belt in the Pacific shows the cutting effect by the Aleutian Islands. The southern belt has reached the southern coast of Australia and revealed the blocking by New Zealand and other Pacific islands. The stretching effect around the gravity depth is visible in the Great Australia Bight where the wave height (in colour green) is lower than those on the deep side (yellow-orange) and near the coastlines (orange-red). This stretching effect is difficult to see in wave models because it is usually muffled up by wind sea and other propagation effects, such as dispersion and refraction.

The lower row (c) of Fig.10 shows the propagation results after 80 hrs. By then the northern belt has cut through the Hawaii Islands, revealing their detailed blocking effects by the 8 main islands. The G25 and SMC25 grids can only resolve 4 islands out of the Hawaii archipelago. The southern belt is now abreast with the northern coast of Australia, pulling through the oceanic islands. The highest 6 km resolution in this SMC6-25 grid is, however, still not enough to show the atolls or coral reefs in the French Polynesian islands as demonstrated by Chawla and Tolman (2008) in a high resolution regional model. So sub-grid obstruction is still required to represent the fine structure. Also note in row (c) of Fig.10, the slow GCT and GSE smoothing effects manifest themselves with the smoothly spreading of wave energy in the Southern Ocean and quickly filling up the shadows behind the wave-blocking islands.

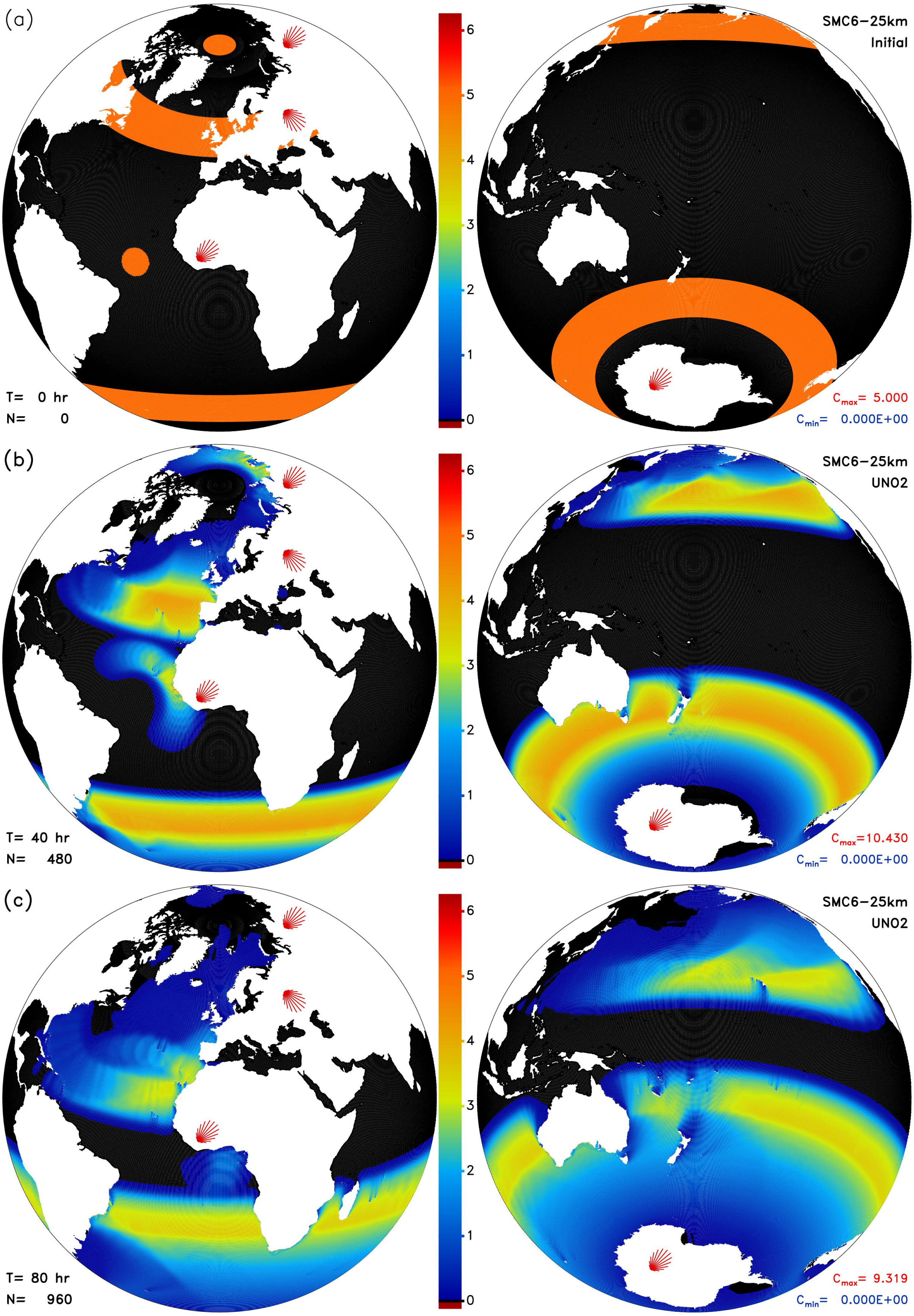

Fig.10. Spectral wave energy propagation on a global SMC 6-25km grid.

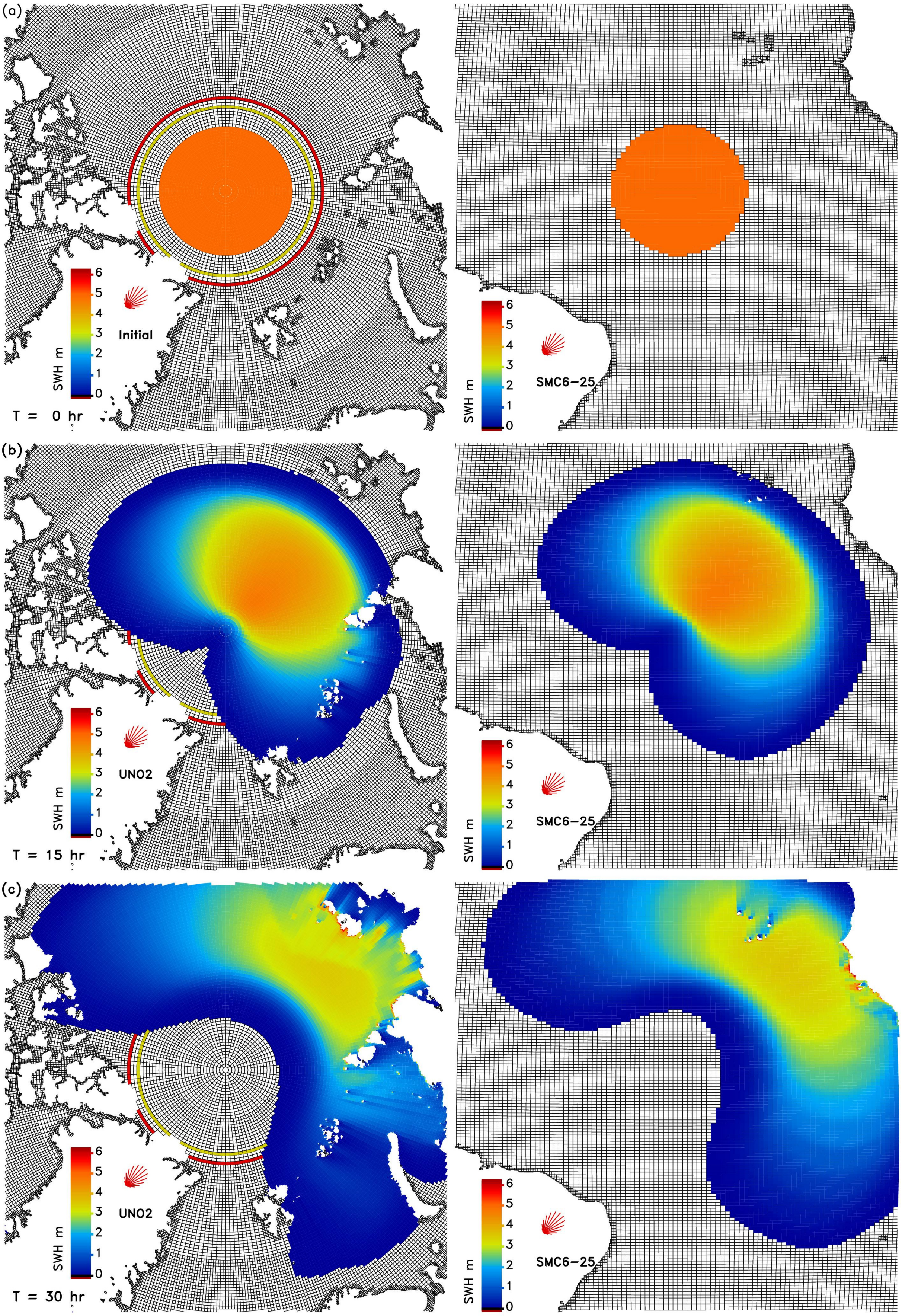

Fig. 11. Comparison of the wave spectral propagation using Arctic map-east (left column) and the conversional local east (right column) reference direction methods.

Because the polar region of the Arctic Ocean is still covered by sea ice, it is not practical to validate the map-east method against wave observations. Here a simple approach is used to assess the map-east method by comparing the propagation of the Arctic and Atlantic patches. As long as the two patches have similar propagation pattern, the map-east method may be considered to be equivalent to the local east method. The two round patches are drawn side-by-side in Fig.11 for this comparison. The row (a) in Fig.11 shows the two initial patches. Because of the different shapes of the grid cells at the two sites, the Arctic patch has a round edge while the Atlantic patch has a stepped edge. Nevertheless, the two patches cover approximately the same surface area. The two co-centred rings in the Arctic part mark the 4 overlapping rows or the transient zone from the local east to the map-east reference directions. The initial spectral peak direction is 45° from their reference direction, respectively, as indicated by the spectral roses.

The middle row (b) of Fig.11 shows the two patches after 15 hrs of propagation. The centre of the Arctic patch has covered the transient zone. It is evident that there is no visible interruption of the wave energy distribution between the two parts and over the 4 overlapping rows. The Arctic patch is quite similar to the Atlantic one shown on the right side except for the fine cuttings caused by local islands. These results confirm that the map-east method in the Arctic part has effectively solved the polar problems and linked smoothly with the global part. The bottom row (c) of Fig.11 shows the two patches after 30 hrs when the Arctic patch is almost out of the map-east zone. The two patches still share a quite close distribution in the deep waters. The blocking effects by local islands and water depth induced refractions have left their unique marks on the two patches. From these results it can be drawn that the map-east method is effective for wave spectral propagation in the polar region and can be used to cover the whole Arctic region if the sea ice disappears in future summers.

5. Summary and conclusions

A 25km single resolution SMC grid (Li 2011) has been installed in the Met Office global wave model, which is adapted from the WAVEWATCH III model (Tolman et al 2002). The SMC grid relaxes the CFL restriction at high latitudes by merging the longitudinal cells and removes the polar singularity by introducing a round polar cell. The map-east reference direction is substituted for the local east direction in the Arctic polar region to define wave spectrum so that the scalar assumption can be maintained. The SMC grid makes it possible to expand global wave models to cover the Arctic in response to the Arctic sea ice retreat in future summers.

Second order upstream non-oscillatory (UNO2) advection scheme (Li 2008) is used for a combined advection-diffusion term. A simple rotation scheme is used for wave spectral refraction and GCT to avoid the CFL restriction of the advection style schemes used for these terms in the original model. The unstructured SMC grid allows all land cells to be removed out of wave propagation schemes, reducing the overall computation time by about 1/3 in comparison with the original latitude-longitude grid model. Ocean surface wave propagation formulations on the sphere are reviewed and a gravity depth is proposed for definition shallow/deep waters. Refraction formulation based on group speed is also derived and compared with the conventional phase speed refraction rate though the present spatial resolution is not enough to this assessment. Validations with satellite and buoy observations show that the SMC grid wave model performs as well as the lat-lon grid model while cutting the total computation time by 1/3.

The SMC grid also permits coastlines and small islands to be resolved at refined resolutions while keeping the open ocean in coarse resolutions. Ocean surface wave spectral energy propagation on a 3-tiered (6-12-25 km) SMC grid is demonstrated to reveal the detailed blocking effects by fine coastal features and small islands. It also illustrates the map-east reference direction method used in an ice-free Arctic. Because of the ice coverage in the Arctic, this map-east method can not be verified with wave observations directly.

References

Ardhuin, F., T.H.C. Herbers, 2005: Numerical and physical diffusion: can wave prediction models resolve directional spread? *J. Atmos. Oceanic Techno*., **22**, 886-895.

Ardhuin, F., T.H.C. Herbers, W.C. O'Reilly, 2001: A hybrid Eulerian-Lagrangian model for spectral wave evolution with application to bottom friction on the continental shelf. *J. Phys. Oceanogr*., **31**, 1498-1516.

Battjes, J.A., 1968: Refraction of water waves. *J. Waterways and Harbors Division*, New York, ASCE, WW4, 437-451.

Booij, N., L.H. Holthuijsen, 1987: Porpagation of ocean waves in discrete spectral wave models. *J. Comput. Phys.*, **68**, 307-326.

Booij, N., R.C. Ris, L.H. Holthuijsen, 1999: A third-generation wave model for coastal regions, 1. Model description and validation. *J. Geophys. Res*. **104**, C4, 7649-7666.

Cavaleri, L., P. Malanotte-Rizzoli, 1981: Wins-wave prediction in shallow water: Theory and applications. *J. Geophys. Res.*, **86**, 10961-10973.

Chawla, A., H.L. Tolman, 2008: Obstruction grids for spectral wave models. *Ocean Modelling*, **22**, 12-25.

Guan, C., V. Rey, P. Forget, 1999: Improvement of the WAM wave model and its application to the Rhone River Mouth area. *J. Coastal Res*., **15**(4), 966-973.

Hardy, T.A., L.B. Mason, J.D. McConochie, 2000: A wave model for the Great Barrier Reef. *Ocean Engineering*, **28**, 45-70.

Holthuijsen, L.H., A. Herman, N. Booij, 2003: Phase-decoupled refraction-diffraction for spectral wave models. *Coastal Engineering*, **49**, 291-305.

Holthuijsen, L.H., H.L. Tolman 1991: Effects of the Gulf Stream on ocean waves. *J. Geophys. Res*., **96**, C7, 12755-12771.

Janssen, P.A.E.M., 2004: *The Interaction of Ocean Waves and Wind*, Cambridge University Press, 300 pp.

Janssen, P.A.E.M., 2008: Progress in ocean wave forecasting. *J. Comput. Phys*., **227**, 3572-3594.

Kinsman, B., 1984: *Wind Waves, their generation and propagation on the ocean surface*. Dover Pub., New York, 676pp.

Leonard, B.P., 1991. The ULTIMATE conservative difference scheme applied to unsteady one-dimensional advection. *Computer Methods Appl. Mech. Eng.* **88**, 17-74.

Li, J.G., 2008: Upstream non-oscillatory advection schemes. *Mon. Wea. Rev*. **136**, 4709-4729.

Li, J.G., 2011: Global transport on a spherical multiple-cell grid. *Mon. Wea. Rev*., **139**, 1536-1555.

Li, J.G., M. Holt 2009: Comparison of ENVISAT ASAR ocean wave spectra with buoys and altimeter data via a wave model. *J. Atmos. Oceanic Techno*., **26**, 593-614.

Longuet-Higgins, M.S., 1957: On the transformation of a continuous spectrum by refraction, *Proc. Cambridge Philosophical Soc*., **53**(1), 226-229.

Nair, R.D., B. Machenhauer, 2002: The mass-conservative cell-integrated semi-Lagrangian advection scheme on the sphere. *Mon. Wea. Rev*., **130**, 649-667.

Phillips, O.M. 1977: *The Dynamics of the Upper Ocean*, Cambridge Univ. Press, Cambridge, 2nd Ed., 336pp.

Rasch, P.J., 1994: Conservative shape-preserving two-dimensional transport on a spherical reduced grid. *Mon. Wea. Rev*., **122,** 1337-1350.

Roe, P.L., 1985: Large scale computations in fluid mechanics. *Lectures in Applied Mathematics* (E. Engquist, S. Osher and R.J.C. Sommerville Eds.), **22**, 163-193.

Tolman, H.L. 1992: Effects of numerics on the physics in a third-generation wind-wave model. *J. Phys. Oceanogr.*, **22**, 1095-1111.

Tolman, H.L. 2002: Alleviating the Garden Sprinkler Effect in wind wave models. *Ocean Modelling*, **4**, 269-289.

Tolman, H.L. 2003: Treatment of unresolved islands and ice in wind wave models. *Ocean Modelling*, **5**, 219-231.

Tolman, H.L., B. Balasubramaniyan, L.D. Burroughs, D.V. Chalikov, Y.Y. Chao, H.S. Chen, V.M. Gerald, 2002: Development and implementation of wind-generated ocean surface wave models at NCEP. *Weather and Forecasting* **17**, 311-333.

Tolman, H.L., D. Chalikov 1996: Source terms in a third-generation wind-wave model. *J. Phys. Oceanogr.*, **26**, 2497-2518.

WAMDI group, 1988: The WAM model - a third generation ocean wave prediction model. *J. Phys. Oceanogr.* **18**, 1775-1810.

WISE Group L. Cavaleri, J.-H.G.M. Alves, F. Ardhuin, A. Babanin, M. Banner, K. Belibassakis, M. Benoit, M Donelan, J. Groeneweg, T.H.C. Herbers, P. Hwang, P.A.E.M. Janssen, T. Janssen, I.V. Lavrenov, R. Magne, J. Monbaliu, M. Onorato, V. Polnikov, D. Resio, W.E. Rogers, A. Sheremet, J. McKee Smith, H.L. Tolman, G. van Vledder, J. Wolf, I. Young, 2007: Wave modelling - the state of the art. *Progress Oceanography*, **75**, 603-674.